energies

MDPI

Article

Energy Production Potential of Ultra-Deep Reservoirs in Keshen Gas Field, Tarim Basin: From the Perspective of Prediction of Effective Reservoir Rocks

Zhida Liu [1,2], Xianqiang Song [2,*], Xiaofei Fu [1,2], Xiaorong Luo [1] and Haixue Wang [1,2]

[1] National Key Laboratory of Continental Shale Oil, Northeast Petroleum University, Daqing 163318, China; lzd6536@163.com (Z.L.)
[2] Laboratory of CNPC Fault Controlling Reservoir, Northeast Petroleum University, Daqing 163318, China
* Correspondence: songxianqiang01@163.com

Abstract: The identification and prediction of effective reservoir rocks are important for evaluating the energy production potential of ultra-deep tight sandstone reservoirs. Taking the Keshen gas field, Tarim Basin, as an example, three distinct petrofacies are divided according to petrology, pores, and diagenesis. Petrofacies, well logs, and factor analysis are combined to predict effective reservoir rocks. We find that petrofacies A has a relatively coarse grain size, moderate mechanical compaction, diverse but low-abundance authigenic minerals, and well-developed primary and secondary pores. It is an effective reservoir rock. Petrofacies B and petrofacies C are tight sandstones with a poorly developed pore system and almost no dissolution. Petrofacies B features abundant compaction-susceptible ductile grains, intense mechanical compaction, and underdeveloped authigenic minerals, while petrofacies C features pervasive carbonate cementation with a poikilotopic texture. We combine well logging with gamma ray, acoustic, bulk density, neutron porosity, resistivity, and factor analyses to facilitate the development of petrofacies prediction models. The models reveal interbedded architecture where effective reservoir rocks are interbedded with tight sandstone, resulting in the restricted connectivity and pronounced reservoir heterogeneity. Classifying and combining well logs with a factor analysis to predict petrofacies provide an effective means for evaluating the energy potential of ultra-deep reservoirs.

Keywords: ultra-deep sandstone gas reservoirs; effective reservoir rock; well logs; factor analysis; tarim basin

check for updates

Academic Editor: Hossein Hamidi

Received: 27 April 2025
Revised: 23 May 2025
Accepted: 30 May 2025
Published: 2 June 2025

Citation: Liu, Z.; Song, X.; Fu, X.; Luo, X.; Wang, H. Energy Production Potential of Ultra-Deep Reservoirs in Keshen Gas Field, Tarim Basin: From the Perspective of Prediction of Effective Reservoir Rocks. *Energies* **2025**, *18*, 2913. https://doi.org/10.3390/en18112913

Copyright: © 2025 by the authors. Licensee MDPI, Basel, Switzerland. This article is an open access article distributed under the terms and conditions of the Creative Commons Attribution (CC BY) license (https://creativecommons.org/licenses/by/4.0/).

1. Introduction

The rapid development of the economy requires more support from oil and gas resources. As such, unconventional and ultra-deep hydrocarbon exploration has attracted attention in the field of petroleum geology [1,2]. Ultra-deep hydrocarbon resources are becoming important for hydrocarbon exploration and development. In clastic formations, ultra-deep reservoirs are characterized by low porosity, low permeability, and small pore throats, with the main reservoir type being tight sandstone [3]. During the deep burial of reservoirs, the diagenetic evolutionary pathway of sandstones is influenced by sedimentation, fluid activity, and the structural framework, resulting in strong pore-scale heterogeneity within reservoirs, which influences the migration and accumulation of hydrocarbons [4–6]. Some sandstones undergo strong diagenesis at early stages, resulting in poor petrophysical properties that form fluid barriers within the reservoir. However, certain sandstones maintain relatively favorable porosity and permeability and can serve

as effective reservoir rocks for ultra-deep sandstone reservoirs. Therefore, identifying and predicting effective reservoir rocks in ultra-deep tight sandstone reservoirs that can accumulate hydrocarbons are key challenges when exploring and developing ultra-deep hydrocarbon reservoirs [7].

The development of effective reservoir rocks may be related to the petrological composition, grain coatings, overpressure, early hydrocarbon charging, dissolution, and fractures in a tight reservoir. A higher rigid grain content reduces porosity loss caused by mechanical compaction in sandstones [8–10]. Well-developed grain coatings (e.g., microcrystalline quartz coatings and authigenic chlorite rims) can inhibit large-scale precipitation of cements on detrital grain surfaces [11–13]. The preservation of pores by overpressure is controlled by the mechanical properties of the sandstone and the relative timing of overpressure development [9]. Overpressure reduces the vertical effective stress on sandstones, reducing mechanical compaction while simultaneously inhibiting intergranular pressure dissolution and hindering silicon ion release, thereby slowing quartz cementation [9]. Early oil charging alters pore water properties and may influence fluid and rock reactions, modifying sandstone wettability [7,14,15]. Hydrocarbon charging in sandstone reservoirs may locally inhibit the precipitation of authigenic diagenetic minerals (e.g., quartz, feldspar, and illite) [14]. Under deep burial conditions, evaporite layers significantly protect primary pores in sandstones. Compared with clastic rocks, evaporite layers exhibit greater thermal conductivity, allowing faster heat transfer from underlying sandstones to the evaporite layer during deep burial. This process results in lower temperatures for sandstones beneath evaporites than for those at equivalent depths without overlying evaporites, thereby retarding cementation processes. The dissolution of unstable detrital components and authigenic minerals under meteoric water, alkaline fluids, or organic acids increases the pore space and improves reservoir quality. Notably, the increase in reservoir porosity during burial diagenesis requires the dissolution of many minerals, and dissolution products need to be transported out of the reservoir by pore water. However, ultra-deep reservoirs are usually relatively closed geological systems. Controlled by the material balance, the development of the scales of dissolution pores and the net increase in sandstone porosity is unrealistic [16]. Thus, dissolution contributes minimally to porosity enhancement in ultra-deep reservoirs lacking preferential migration pathways (e.g., faults, fractures, or unconformities). Fractures may increase the reservoir space of tight reservoirs, to a certain extent; however, more importantly, the development of fractures can greatly increase the permeability of low-permeability and tight reservoirs and provide an advantageous migration channel for fluids [17–19]. Although all the above mechanisms are conducive to the formation of effective reservoir rocks, the types of effective reservoir rocks in ultra-deep tight sandstone gas reservoirs have not yet been clearly defined.

Owing to cost constraints and safety risks, core samples are typically drilled from only a limited number of wells during practical oil and gas exploration, with restricted sampling depths and ranges. Consequently, core samples can record information only from localized strata within hydrocarbon reservoirs. It is impossible to comprehensively understand reservoir characteristics and predict effective reservoir rocks solely through core analysis. To investigate the spatial configuration of effective reservoir rocks within reservoirs on a broader scale, well log data are essential. Well log data capture critical information about formation fluid properties, petrological composition, porosity, and other key parameters are among the most important tools for understanding formation characteristics [20–22]. Based on the distinct logging responses of various characteristic rocks in tight sandstone reservoirs, log-based methods of identification can be established to differentiate between effective and noneffective reservoir rocks. This approach provides evidence supporting the evaluation of ultra-deep tight sandstone reservoir quality [21].

The Tarim Basin is one of the most resource-rich basins in China for ultra-deep oil and gas [23]. Within the basin, the Keshen gas field serves as a representative ultra-deep gas reservoir, with its natural gas resources having been estimated at approximately one trillion cubic meters. Within this field, the Cretaceous Bashijiqike Formation (K_1bs) serves as a key ultra-deep tight sandstone gas reservoir. Overall, the Bashijiqike Formation has experienced intense diagenetic alteration, high compaction, and extremely low porosity and permeability. However, the prediction and types of effective reservoir rocks capable of hosting hydrocarbon accumulation in ultra-deep tight sandstone reservoirs remain poorly constrained. The aims of this study are as follows: (1) to classify tight sandstones based on pore-scale characteristics and define effective reservoir rock types within ultra-deep tight sandstone reservoirs, and (2) to develop a predictive framework for identifying effective reservoir rocks by integrating sandstone lithotype classification, well log response analysis, and factor analysis.

2. Geological Background

The Tarim Basin, located in northwestern China (Figure 1a), has exceptionally abundant geological resources. The Keshen gas field lies within the Kuqa Depression of the Tarim Basin (Figure 1b). The Kuqa Depression extends in an ENE-trending direction. It is approximately 550 km wide from east to west, 30–80 km wide from south to north and covers an area of approximately 28,500 km^2 (Figure 1b). The Kuqa Depression is a Meso-Cenozoic superimposed foreland basin developed based on a Paleozoic passive continental margin [24]. The development of the Kuqa Depression initiated during the late Hercynian period and has undergone three major tectonic phases since the late Permian, resulting in complex evolutionary processes: the late Permian–Triassic foreland basin stage, the Paleogene extensional depression basin stage, and the Neogene–Quaternary intracontinental foreland basin stage [25]. The Himalayan orogeny exerted the most intense tectonic influence on the Kuqa Depression, during which intense compressional thrusting occurred, forming a series of large thrust–nappe structures along the southern Tianshan front. These tectonic activities further shaped three structural belts (Kelasu, Yiqikelike, and Qiulitage), two slope zones (northern and southern), and three sags (Wushi, Baicheng, and Yangxia) [26]. The stratigraphy of the Kuqa Depression is composed of predominantly Mesozoic and Cenozoic strata [27]. The Baicheng Sag and Yangxia Sag are the primary hydrocarbon-generating sags and host two types of source rocks: lacustrine and coal-measure [28]. The stratigraphic sequence of the Kuqa Depression is shown in Figure 2. Lacustrine source rocks are represented by the Upper Triassic Huangshanjie Formation (T_3h) and Middle Jurassic Qiakemake Formation (J_2q), whereas coal-measure source rocks include the Upper Triassic Tariqi Formation (T_3t), Lower Jurassic Yangxia Formation (J_1y), and Middle Jurassic Kezilenuer Formation (J_2k). The Kuqa Depression contains multiple clastic reservoirs, such as the Jurassic Ahe Formation (J_1a) and Yangxia Formation (J_1y), the Cretaceous Bashijiqike Formation (K_1bs) and Shushanhe Formation (K_1s), and the Paleogene Suweiyi Formation (E_3s) [28]. Of these formations, the Cretaceous Bashijiqike Formation is among the most significant gas-bearing reservoirs in the Kuqa Depression.

The Kelasu Structural Belt, situated in the central Kuqa Depression, generally exhibits a nearly E–W-trending orientation [29]. The Keshen gas field (Figure 1c) is located within this belt. Under intense N–S compression during the Himalayan period, the Kelasu Structural Belt developed a series of north-dipping thrust faults, which combined with strata to form geological structures, such as anticlines and faulted anticlines [30]. These thrust faults act as critical pathways for hydrocarbon migration and accumulation, facilitating the migration of oil and gas from source rocks to structural traps through fault systems. The Cretaceous Bashijiqike Formation serves as the primary reservoir for the Keshen gas field

(Figure 2) and was deposited under hot and arid climatic conditions [27]. The third member (K_1bs^3) corresponds to a fan delta front subfacies, whereas the first and second members (K_1bs^2 and K_1bs^1) are characterized by braided river delta front subfacies [31]. During the middle Cretaceous, the Keshen area underwent uplift, leading to a certain degree of erosion at the top of the first member of the Cretaceous Bashijiqike Formation [32]. At present, the burial depth of the Cretaceous Bashijiqike Formation reservoirs in the Keshen gas field generally exceeds 5500 m, with the deepest sections reaching approximately 8000 m. The Cretaceous Bashijiqike Formation is overlain by the Paleogene Kumugeliemu Group gypsum–salt layers, which exceed 1500 m in thickness across most regions [27]. These massive gypsum–salt layers provide excellent sealing caps for Cretaceous reservoirs [22]. In general, the Keshen area is compartmentalized by thrust faults into low-relief fault anticlines. Hydrocarbon exploration has revealed that the core areas of these anticlines are the primary zones for natural gas enrichment.

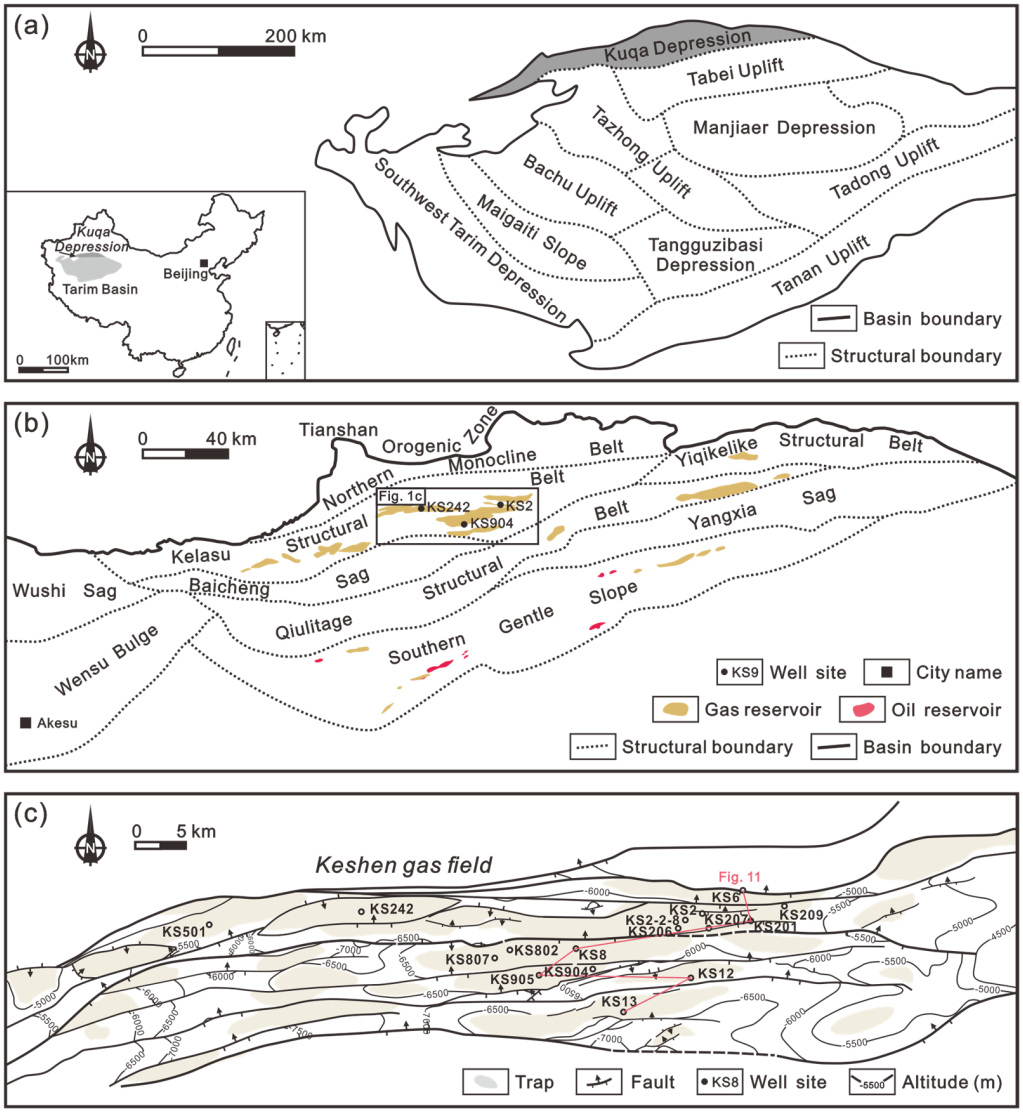


Figure 1. (**a**) Structural units of the Tarim Basin, China; (**b**) structural units in the Kuqa Depression; (**c**) structural characteristics of the Keshen gas field; The location of wells in Figure 11 is shown in Figure 1c.

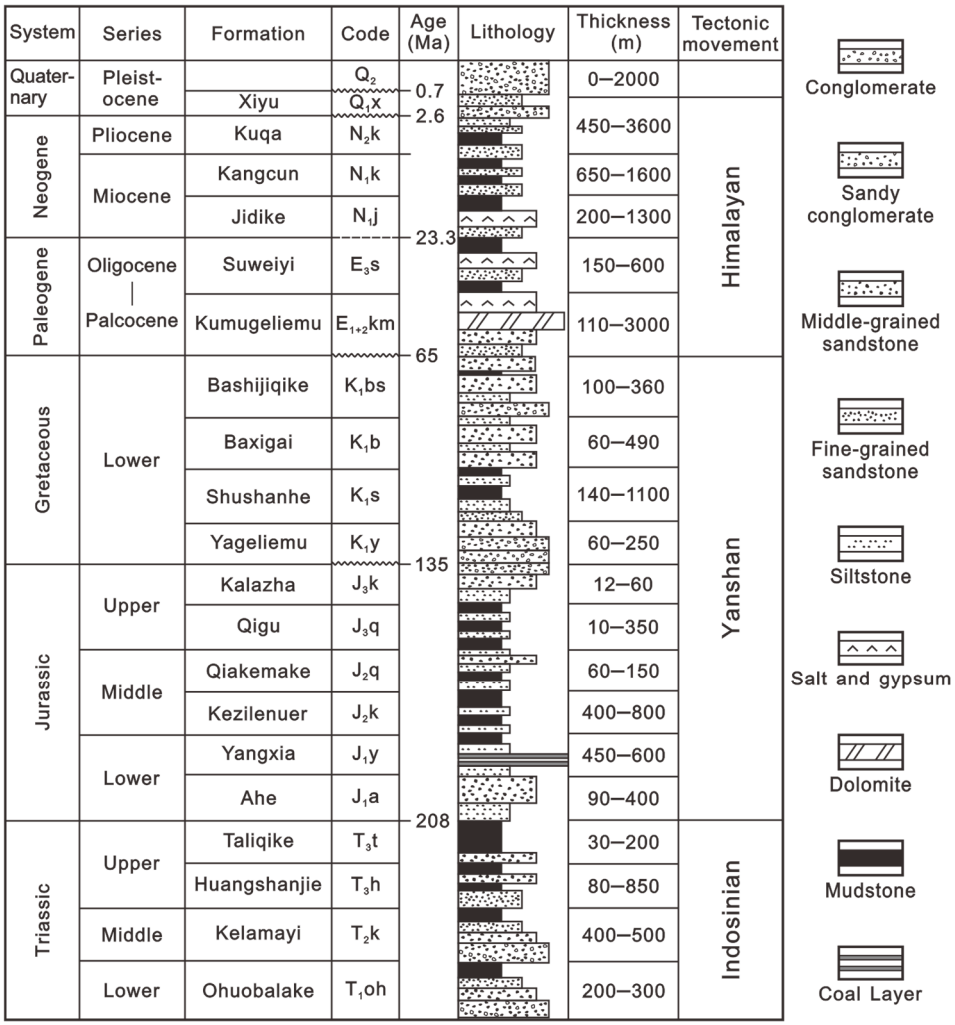


Figure 2. Comprehensive stratigraphic diagram of the Kuqa Depression (modified from [27]).

3. Materials and Methods

3.1. Core Observation and Petrological Analysis

Core observations were carried out in 12 selected cored wells within the Cretaceous Bashijiqike Formation of the Keshen gas field in the Tarim Basin, where the cores exhibited relatively intact preservation and longer coring intervals. Using these cores, the characteristics of the Cretaceous Bashijiqike Formation were analyzed, with detailed observations and descriptions of the color, lithology, texture, sedimentary structure, and bedding of the sandstone. We selected sandstone samples with changed petrological characteristics based on core observations. The intervals between samples in each well were approximately between 10 cm and 50 cm. In total, 226 representative sandstone samples were selected to conduct a variety of microscopic observations, including those of optical thin sections impregnated with blue epoxy resin, scanning electron microscopy (SEM), and cathodoluminescence (CL). Then, 226 pieces of optical thin sections were prepared by selecting sandstones with different petrological characteristics. The optical thin sections were treated with Alizarin Red S and K-ferricyanide to distinguish carbonate minerals. A Zeiss Axio Z1 optical microscope was used with the equidistant point-counting method to quantitatively analyze and statistically evaluate detrital grains, interstitial materials, pores, and their proportions within thin sections. This process clarified the detrital mineralogy, interstitial components, and types of authigenic minerals in the sandstone, analyzed the types and proportions of pores, and investigated the sequential relationships between different authigenic minerals

and dissolution. The detrital textures of the sandstone, including the grain size, sorting, and roundness, were further analyzed by integrating optical thin sections with the ImageJ v1.0 software. An FEI Quanta 450 scanning electron microscopy (SEM) (FEI Company, Hillsboro, OR, USA) instrument was used in both secondary electron (SE) (11 sandstone samples) and backscattered electron (BSE) modes (9 sandstone samples) to analyze the types and growth sequences of the authigenic minerals in the sandstone. This method was combined with energy-dispersive spectroscopy (EDS) to qualitatively determine the chemical composition of the authigenic minerals. A Cl8200 MK5-2 cathodoluminescence system (Cambridge Image Technology Ltd, Cambridge, UK) was used to observe the stages and characteristics of carbonate minerals in 10 sandstone samples. The petrological composition of the 226 sandstone samples is summarized in Table 1.

Table 1. Thin-section point-counting data of ultra-deep K_1bs sandstone.

Content	Detrital Mineralogy						
	Quartz	K-Feldspar	Plagioclase	Sedimentary Rock Fragment	Metamorphic Rock Fragment	Volcanic Rock Fragment	Mica
Average (%)	44	18	10	4	13	10	0.3
Range (%)	37–57	8–26	3–18	2–10	6–25	4–17	0–2
Content	**Mud-Matrix**	**Cement (%)**					
		Calcite	**Dolomite**	**Fe-Dolomite**	**Authigenic Quartz**	**Anhydrite**	**Authigenic Albite**	**Hematite**
Average (%)	3.8	3.6	1.6	0.2	0.9	0.2	0.7	0.06
Range (%)	0–20	0–26	0–35	0–3	0–4	0–3	0–3	0–4

As microscopic analyses do not allow for quantitative determination of the content of clay minerals in sandstone samples, a Bruker D8 X-ray diffraction (XRD) analyzer was used to analyze the types and abundances of clay minerals in 93 sandstone samples quantitatively. The results of the XRD are shown in Table 2. Based on the petrology and diagenesis of sandstone, petrofacies within ultra-deep tight sandstone reservoirs can generally be categorized into effective reservoir rocks and tight petrofacies.

Table 2. XRD data of ultra-deep K_1bs sandstone.

Total Content of Clay Minerals (%)	Relative Content of Different Types of Clay Minerals (%)							
	Mixed-Layer Illite/Smectite		Illite		Kaolinite		Chlorite	
	Average	Range	Average	Range	Average	Range	Average	Range
2–30	31.5	0–71	57.4	17–86	3.5	0–18	7.6	1–25

A total of 153 sandstone plug samples with a diameter of 25 mm and a length of 50 mm were drilled, and a confining pressure porosity and permeability tester was employed to measure the porosity and permeability of the sandstone samples. This technique allowed for a comparative analysis of the petrophysical property conditions among different sandstone samples.

3.2. Prediction of Effective Reservoir Rocks Using Well Logging

When identifying effective reservoir rocks and tight petrofacies in ultra-deep tight sandstone reservoirs through well logging, owing to the difference in the weights of well logging instruments in the same well, the tension during the descent of the instrument into the well is different, resulting in errors in depth among different well log data. To ensure

depth consistency across different types of well logs, depth correction was first applied to different well logs from the same well. A well log curve with distinct characteristics was selected as the reference curve, and its prominent feature positions were used as markers to adjust the depths of other well log curves in the well. This process began by comparing core lithology with well log response characteristics to select one well log curve that exhibits strong lithological correlation as the reference curve for depth correction. Stable intervals within the reference curve, where the lithology and well log responses remain consistent, were designated as marker intervals. These marker intervals were then utilized to perform depth corrections on other well log curves. After depth correction, the response characteristics of all well log curves at the same depth within the well exhibited uniformity in reflecting rock properties. Well log curves of the same type from different wells were standardized, such that well log curves of the same type exhibited comparable ranges across different wells. The fundamental basis for well log curve standardization lies in the geological principle that similar sedimentary environments produce comparable rock types and corresponding well log responses.

Additionally, due to factors such as core loss or core recovery rates during coring operations, discrepancies may exist between the marked burial depths of cores in cored wells and the recorded burial depths of well log curves. Therefore, to align cored intervals with their corresponding well log responses, it was necessary to verify the consistency between cores and well log data in cored wells and apply depth corrections to mismatched cores. Comparing the lithology interpreted from well logs and the response characteristics of well log curves to geological layers, the burial depths of cored intervals were adjusted through multiple types of well log curve analyses. This adjustment ensures that the well log responses accurately matched the petrological variations observed in the cores.

3.3. Factor Analysis of the Well Log Responses

Referring to prior studies that utilized mathematical approaches for dimensionality reduction in multiple well log datasets [33], in this research, five types of well logs sensitive to petrological composition and petrophysical properties were selected: gamma ray (GR), acoustic (AC), bulk density (DEN), compensated neutron (CNL), and resistivity (RD) logs. Factor analysis was employed to process the well logs. Given the substantial variations in data ranges across different well logs, normalization was performed on them, providing datasets to standardize these inputs for factor analysis.

4. Results

4.1. Sandstone Petrology

4.1.1. Detrital Texture and Mineralogy

Core observations reveal that the tight sandstone reservoirs consist of predominantly reddish brown and grayish white siltstone, fine-grained sandstone, medium-grained sandstone, medium- to coarse-grained sandstone, and dark-red mudstone, with medium- and fine-grained sandstones constituting the dominant lithologies. The sandstone reservoirs are characterized primarily by massive bedding. The medium-grained sandstones exhibit trough cross-bedding formed by vertical accumulation at the lower cutbank of the river channel and tabular cross-bedding resulting from lateral or downstream channel accretion. The medium-grained sandstones display through cross-bedding generated through lateral channel accretion and tabular cross-bedding formed by lateral or downstream accretion. The fine-grained sandstones feature parallel bedding and tabular cross-bedding, whereas the siltstone–sandstones feature predominantly parallel bedding. The locally observed argillaceous gravels within the sandstones are irregular, torn, or angular.

Through identification via optical thin-section point counting, it has been determined that the sandstone lithologies include two types, namely, lithic arkose and feldspathic litharenite, with lithic arkose being the predominant variety (Table 1). The detrital quartz is predominantly monocrystalline quartz, with relative contents ranging from 37% to 58%, with an average value of 44% (Table 1). The detrital feldspar contents vary between 18% and 40%, for an average of 30%, comprising K-feldspar contents of 8–30% (average of 19%) and relative plagioclase contents ranging from 3% to 19% (average of 11%) (Table 1). The lithic fragment contents range from 13% to 37%, with a mean value of 26% (Table 1). Among lithic components, both metamorphic and volcanic rock fragments exhibit higher relative abundances than sedimentary rock fragments do, with metamorphic rock fragments predominating. Metamorphic rock fragments display relative contents of 5–25% (average of 12%), consisting of primarily low-grade metamorphic rock fragments and quartz fragments. Volcanic rock fragments have relative contents of 3–17% (average of 10%). Sedimentary rock fragments occur in smaller quantities, ranging from 1% to 10%, with an average of 4% (Table 1), and are composed of predominantly mudstone fragments. Trace amounts of mica are observed within detrital grains, with the relative mica contents remaining less than 1% in most sandstones.

4.1.2. Interstitial Material

The analysis of optical thin section, scanning electron microscopy (SEM), and clay mineral X-ray diffraction (XRD) data confirms that the sandstones host a variety of interstitial materials. The matrix is predominantly argillaceous, accounting for 0–20% of the total rock volume, whereas the cement types include calcite, dolomite, authigenic quartz, anhydrite, authigenic feldspar, clay minerals, and hematite. Carbonate cements dominate volumetrically, with calcite contents ranging from 0 to 26% (average of 3.6%) and dolomite accounting for 35% (average of 1.6%). Ferroan dolomite occurs in minor quantities (<3%). Authigenic quartz generally does not exceed 4% (average of 0.9%). Regionally, the reservoir in the northern Keshen gas field has a relatively high calcite content and low dolomite abundance, whereas dolomite prevails in carbonate cements in the southern area. Authigenic quartz contents range from 0 to 4% (average of ~0.9%). Trace anhydrite cement (0–3%, average of 0.2%) is observed in the sandstone pores and is stratigraphically concentrated in K_1bs^1, followed by K_1bs^2, and it is minimal in K_1bs^3. Authigenic albite, present as feldspar overgrowths and euhedral columnar crystals, constitutes 0–3% (average of 0.83%). The hematite contents remain at less than 4.3% (average of 1–2%). The XRD data are summarized in Table 2. They indicate total clay mineral contents of 2–30% in the sandstones, dominated by illite (17–86%, average of 57.4%), followed by mixed-layer illite/smectite (0–71%, average of 31.5%), chlorite (1–25%, average of 7.6%), and trace kaolinite (0–2.24%, average of 0.23%). This mineralogical distribution highlights strong illitization within the reservoir and extensive kaolinite alteration, with clay assemblages reflecting a predominance of illite and mixed-layer illite/smectite over chlorite and kaolinite.

4.2. Effective Reservoir Rock and Tight Petrofacies

4.2.1. Petrofacies Classification in Ultra-Deep Tight Sandstone Reservoirs

The reservoir in the Keshen gas field is composed of multiple sand bodies superimposed between argillaceous rocks. As shown in Figure 3, the petrological composition, porosity, and permeability of sandstone within the sand body are variable, showing heterogeneity. A comparative analysis of the petrological characteristics reveals that sandstones with coarser grain sizes, higher contents of rigid grains (such as quartz and feldspar), and lower contents of ductile grains (including clay matrix, altered volcanic rock fragments, low-grade metamorphic rock fragments, and mica) tend to develop relatively abundant

pore spaces and demonstrate better petrophysical properties, such as the sandstone buried at a depth of 5626.1 m in Well KS6 (Figure 4a). Conversely, sandstones dominated by fine-grained rocks with high ductile grain contents and significant compactive deformation of rock fragments exhibit poorer petrophysical properties, such as the sandstone buried at a depth 5628.2 m in Well KS6 (Figure 4b). As also shown in Figure 3, the sandstone buried at a depth of 5621.7 m in Well KS6 has a calcite content of 25%. Petrological evidence suggested that the precipitation of extensive carbonate minerals in sandstone has consumed the pore spaces, and the thin-section porosity is only about 1% (Figure 4c). It is indicated that extensive carbonate minerals result in localized tight sandstone with extremely poor reservoir quality (Figure 4c).

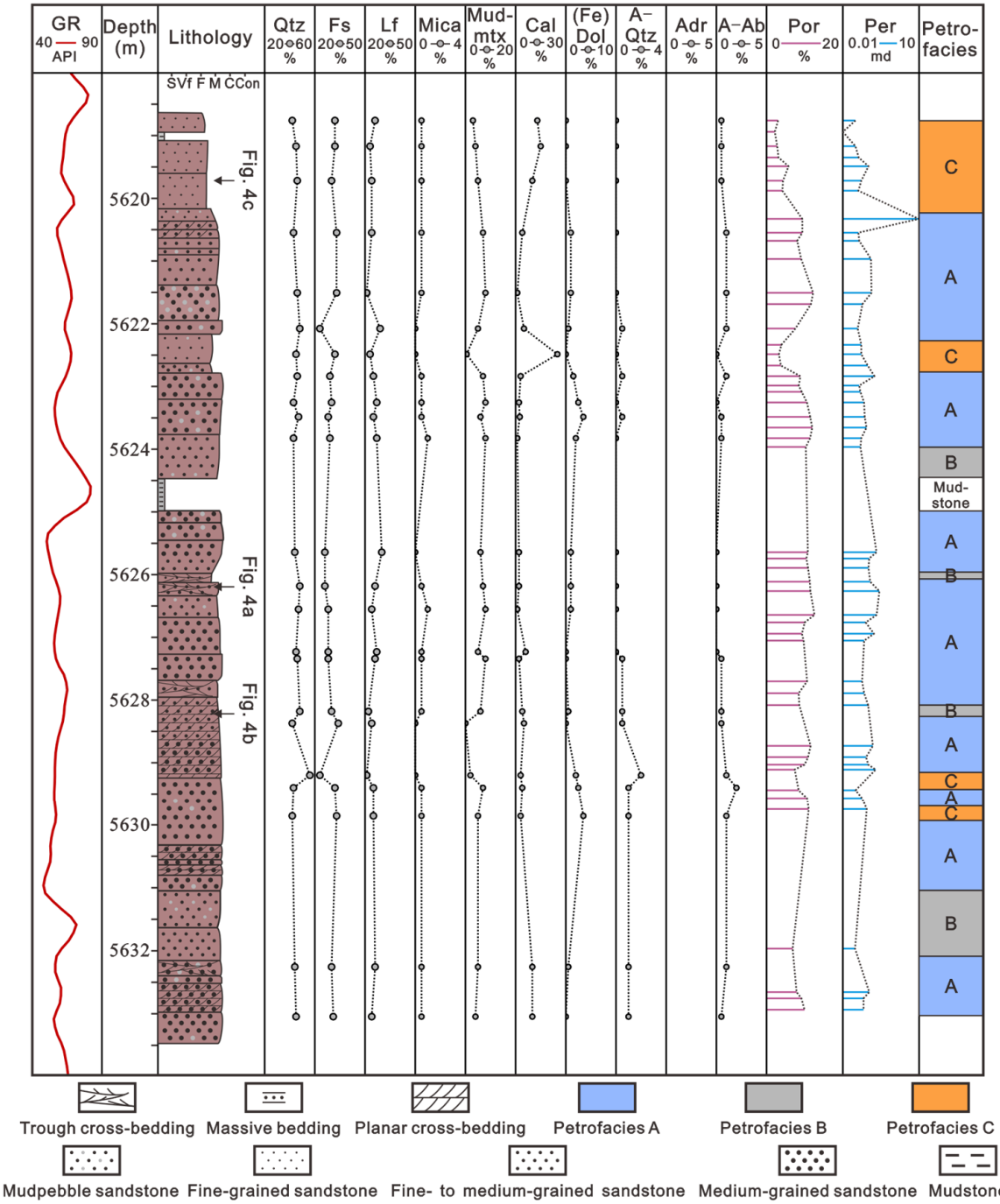


Figure 3. Mineralogy, petrophysical properties and petrofacies of K_1bs in Well KS6. Qtz: quartz; Fs: feldspar; Lf: lithic fragment; Mud-mtx: mud-matrix; Cal: calcite; (Fe) Dol: (Fe) dolomite; A-Qtz: authigenic quartz; Adr: anhydrite; A-Ab: authigenic albite; Por: porosity; Per: permeability.

Therefore, based on variations in sandstone lithofacies, petrological composition and texture, diagenesis, and pore characteristics, the heterogeneous tight sandstone reservoirs are categorized into three petrofacies: (1) petrofacies A, i.e., ductile grain-poor sandstone (Figure 4a), (2) petrofacies B, i.e., ductile grain-rich sandstone (Figure 4b), and (3) petrofacies C, i.e., carbonate–tightly cemented sandstone (Figure 4c). In this study, ductile grains refer to detrital grains that exhibit significant bending deformation under microscopic observation, and these grains include primarily altered volcanic rock fragments, low-grade metamorphic rock fragments, mica, and mudstone fragments. These ductile grains undergo pronounced deformation under compaction, demonstrating characteristic bending features that encroach into pore spaces. The carbonate cements are dominated by calcite and dolomite.

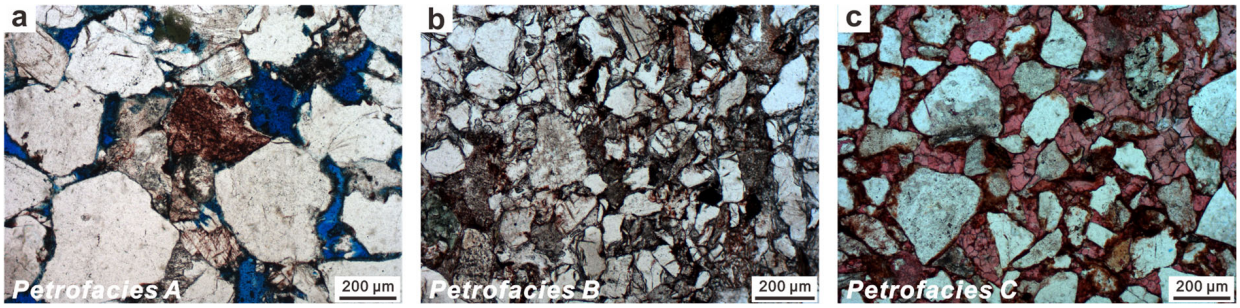


Figure 4. Micrographs of different petrofacies in K_1bs ultra-deep tight sandstone reservoirs: (**a**) ductile grain-poor sandstone (petrofacies A), with blue color denoting pore spaces, Well KS6, 5626.1 m; (**b**) ductile grain-rich sandstone (petrofacies B), Well KS6, 5628.2 m; (**c**) carbonate–tightly cemented sandstone (petrofacies C), Well KS6, 5621.7 m.

4.2.2. Petrology of the Effective Reservoir Rock and Tight Petrofacies

Different petrofacies exhibit marked differences in detrital texture and mineralogy, as well as in the types and contents of interstitial materials, which are summarized in Figure 5 and Table 3.

Differences in Detrital Textures and Mineralogies Among Different Petrofacies

Petrofacies A is characterized primarily by a high rigid grain content, low ductile grain content, low cement content, relatively coarse grain size, and high thin-section porosity. As shown in Figure 4a, the thin-section porosity is approximately 9%. The relative contents of quartz range from 38% to 56%, those of feldspar range from 23% to 39%, those of rock fragments range between 15% and 33%, those of mica range from approximately 0 to 1% (Figure 5a), those of matrix range from approximately 0 to 10% (Figure 5b), and those of ductile grains range from 7.5% to 19% (Table 3). The ductile grain-poor sandstone comprises mainly medium-grained sandstones, with median grain sizes ranging from 0.14 mm to 0.4 mm (Figure 6a, Table 3). The grain contacts are predominantly point-to-line types, indicating a grain-supported texture (Figure 4a).

Petrofacies B is characterized by a high ductile grain content, low cement content, relatively fine grain size, and low porosity in thin sections (Figure 4b). It comprises predominantly fine-grained sandstones with median grain sizes ranging from 0.08 mm to 0.3 mm (Figure 6b). The relative contents of detrital quartz range from 37% to 55%, those of feldspar range from 18% to 37%, those of rock fragments range between 25% and 36%, those of mica range from approximately 0 to 2% (Figure 5c), and those of matrix range from approximately 0.5% to 20% (Figure 5d, Table 3). Overall, the ductile grain contents range from 16% to 33.5%, and the cement contents range from 0% to 9% (Table 3).

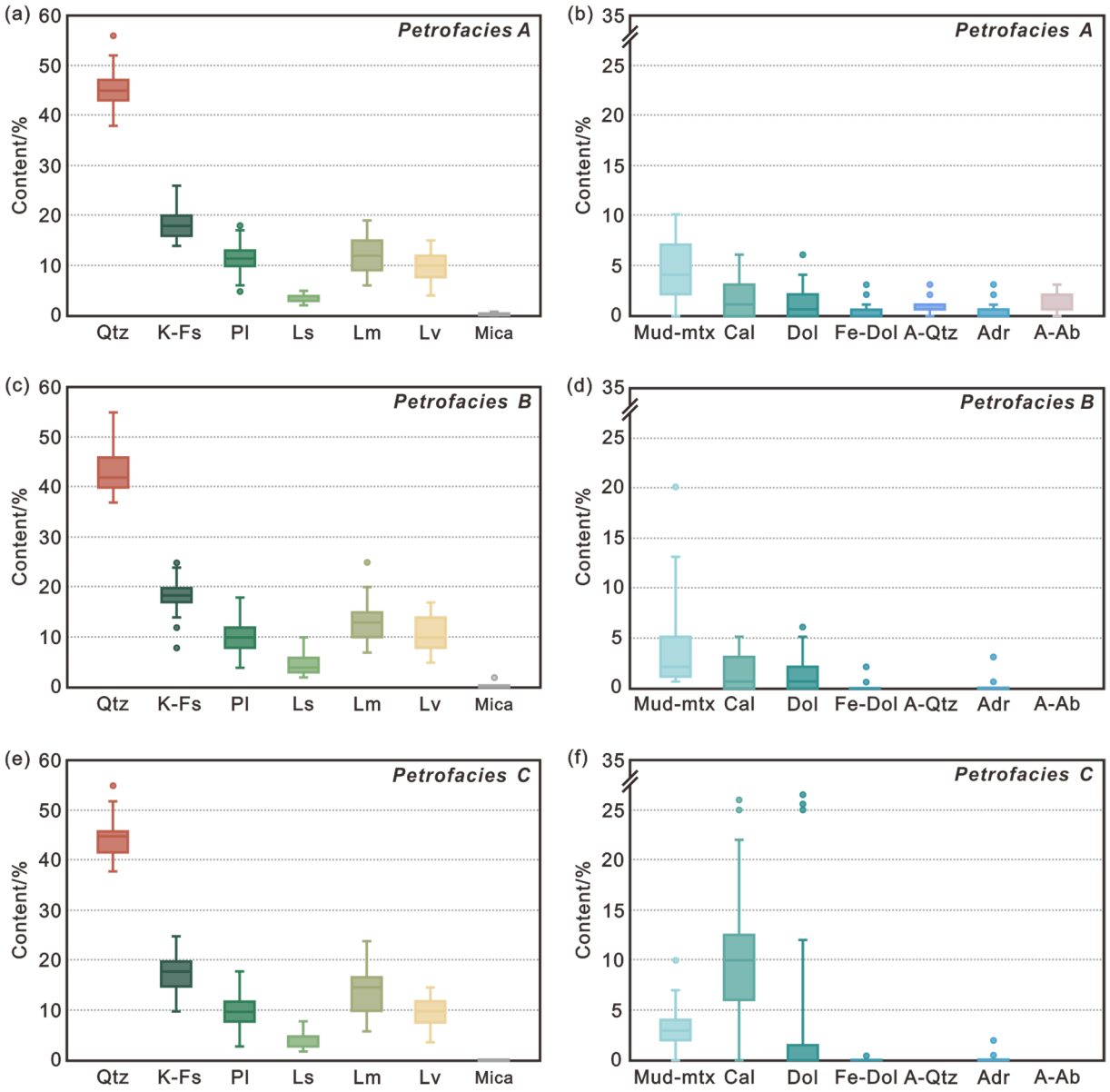


Figure 5. Petrology of different petrofacies of the K_1bs ultra-deep tight sandstone reservoirs: (**a**) detrital grain content in petrofacies A; (**b**) content of interstitial material in petrofacies A; (**c**) detrital grain content in petrofacies B; (**d**) content of interstitial material in petrofacies B; (**e**) detrital grain content in petrofacies C; (**f**) content of interstitial material in petrofacies C. Qtz: quartz; K-fs: K-feldspar; Pl: plagioclase; Ls: sedimentary rock fragment; Lm: metamorphic rock fragment; Lv: volcanic rock fragment; Mud-mtx: mud-matrix; Cal: calcite; Dol: dolomite; Fe-Dol: Fe-dolomite; A-Qtz: authigenic quartz; Adr: anhydrite; A-Ab: authigenic albite.

Petrofacies C features a low ductile grain content, high carbonate cement content, and low thin-section porosity (Figure 4c). The carbonate cements are dominated by calcite or dolomite, exhibiting matrix-supported cementation under microscopic observation. The relative contents of detrital quartz range from 38% to 57%, those of feldspar range from 19% to 36%, those of total rock fragments range between 17% and 37%, those of mica range from approximately 0 to 0.5% (Figure 5e), and those of matrix range from approximately 0 to 10% (Figure 5f, Table 3). Overall, the ductile grain contents range from 10% to 18% (Table 3). The carbonate-cemented tight sandstones in the Bashijiqike Formation display a wide grain size distribution, with median grain sizes varying from 0.16 mm to 0.38 mm (Figure 6c, Table 3).

Table 3. Quantitative petrological statistics in effective reservoir rocks (petrofacies A) and tight petrofacies (petrofacies B and petrofacies C).

Petrofacies	Quartz (%)	Feldspar (%)	Rock Fragment (%)	Mica (%)	Mud-Matrix (%)	Total Cement (%)	Carbonate Minerals (%)	Ductile Grain (%)	Median Grain Size (%)	Thin-Section Porosity (%)
A	38–56	23–39	15–33	0–1	0–10	1–10.5	1–7	8–19	0.14–0.4	1–8.3
B	37–55	18–37	25–36	0–2	0.5–20	0–9	0–7	16–34	0.08–0.3	0–1.1
C	38–57	19–36	17–37	0–0.5	0–10	10–35	10–35	10–18	0.16–0.38	0–1

Petrofacies	Calcite (%)	Dolomite (%)	Fe-Dolomite (%)	Authigenic Quartz (%)	Anhydrite (%)	Authigenic Albite (%)
A	0–6	0–6	0–3	0–3	0–3	0–3
B	0–5	0–6	0–2	-	0–3	-
C	0–26	0–35	0–0.5	-	0–2	-

Petrofacies	Total Content (%)	Relative Content (%)			
		Mixed-Layer Illite/Smectite	Illite	Kaolinite	Chlorite
A	2–13	0–60	38–84	1–14	1–25
B	3–30	11–66	26–75	1–9	3–13
C	2–4	0–71	17–84	0–16	3–17

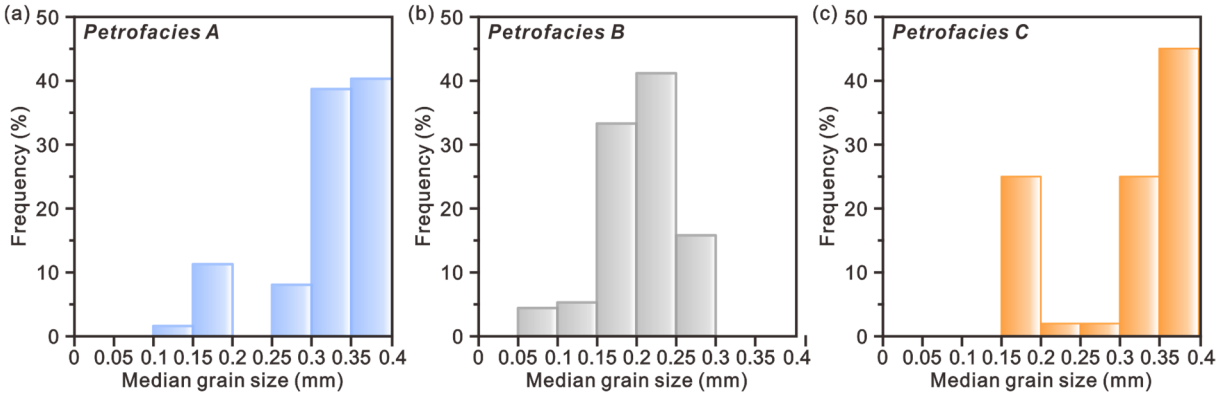


Figure 6. Distribution of median grain sizes in different petrofacies of sandstones: (**a**) petrofacies A; (**b**) petrofacies B; (**c**) petrofacies C.

Interstitial Material in Different Petrofacies

Various types of cements precipitated in petrofacies A, although their abundance is relatively low (Table 3). The total cement contents in this petrofacies range from 1% to 10.5%, with minerals comprising primarily calcite, dolomite, ferroan dolomite, authigenic quartz, anhydrite, and authigenic feldspar (Figure 5b). Specifically, the calcite contents range from 0 to 6%, the dolomite contents range from 0 to 6%, the ferroan dolomite contents range from 0 to 3%, the authigenic quartz contents range from 0 to 3%, and the authigenic feldspar contents range from 0 to 3% (Figure 5b, Table 3). The total clay mineral contents range from 2% to 13%, dominated by mixed-layer illite/smectite, illite, and chlorite, with microscopic observations, indicating negligible kaolinite.

Petrofacies B has a lower cement content and fewer cement types than ductile grain-poor sandstones do, with clay minerals serving as the primary cements (Table 3). The total cement contents range from 0 to 9%, with minerals including calcite, dolomite, ferroan dolomite, anhydrite, hematite, and clay minerals. Authigenic quartz and feldspar are absent (Figure 5d). The calcite contents are 0–5%, the dolomite contents are 0–6%, the ferroan dolomite contents are 0–2%, and the anhydrite contents are 0–3% (Figure 5d, Table 3). The clay mineral contents increase significantly to 3–30% (Table 3).

Petrofacies C has a relatively high cement content dominated by carbonate minerals, with limited diversity in cement types. The total cement contents range from 10% to 35%, being entirely composed of carbonate minerals (Figure 5f). Trace amounts of hematite (0–0.5%), ferroan dolomite (0–0.5%), and anhydrite (<2%) are occasionally observed. The calcite contents range from 0 to 26%, the dolomite contents range from 0 to 35%, and the clay mineral contents decrease markedly to 2–4% (Figure 5f, Table 3).

4.2.3. Diagenesis of Effective Reservoir Rocks and Tight Petrofacies

We analyzed the diagenesis of different petrofacies, as presented in Figure 7. Petrofacies A has a high content of rigid grains, with relatively strong resistance to compaction and moderate mechanical compaction. Early diagenesis did not involve extensive carbonate cementation, allowing for frequent fluid activity. Multiple stages of diagenesis occurred during burial. Authigenic minerals are diverse but low in total abundance, with petrological evidence indicating the precipitation of carbonate minerals (Figure 7a), authigenic quartz (Figure 7b), authigenic albite (Figure 7c), anhydrite, authigenic clay minerals (Figure 7d), and hematite (Table 3) within pores.

Petrofacies B has abundant highly compactible ductile grains (Figure 7e) and is characterized by poor compaction resistance. During early diagenesis, significant pore loss due to mechanical compaction results in limited fluid activity and relatively simple diagenetic

processes. Pores contain only minor amounts of calcite, dolomite (Figure 7f), anhydrite, and hematite, with clay minerals dominating authigenic minerals (Figure 7g). Almost no dissolution occurs, and dissolution pores are almost invisible in thin sections.

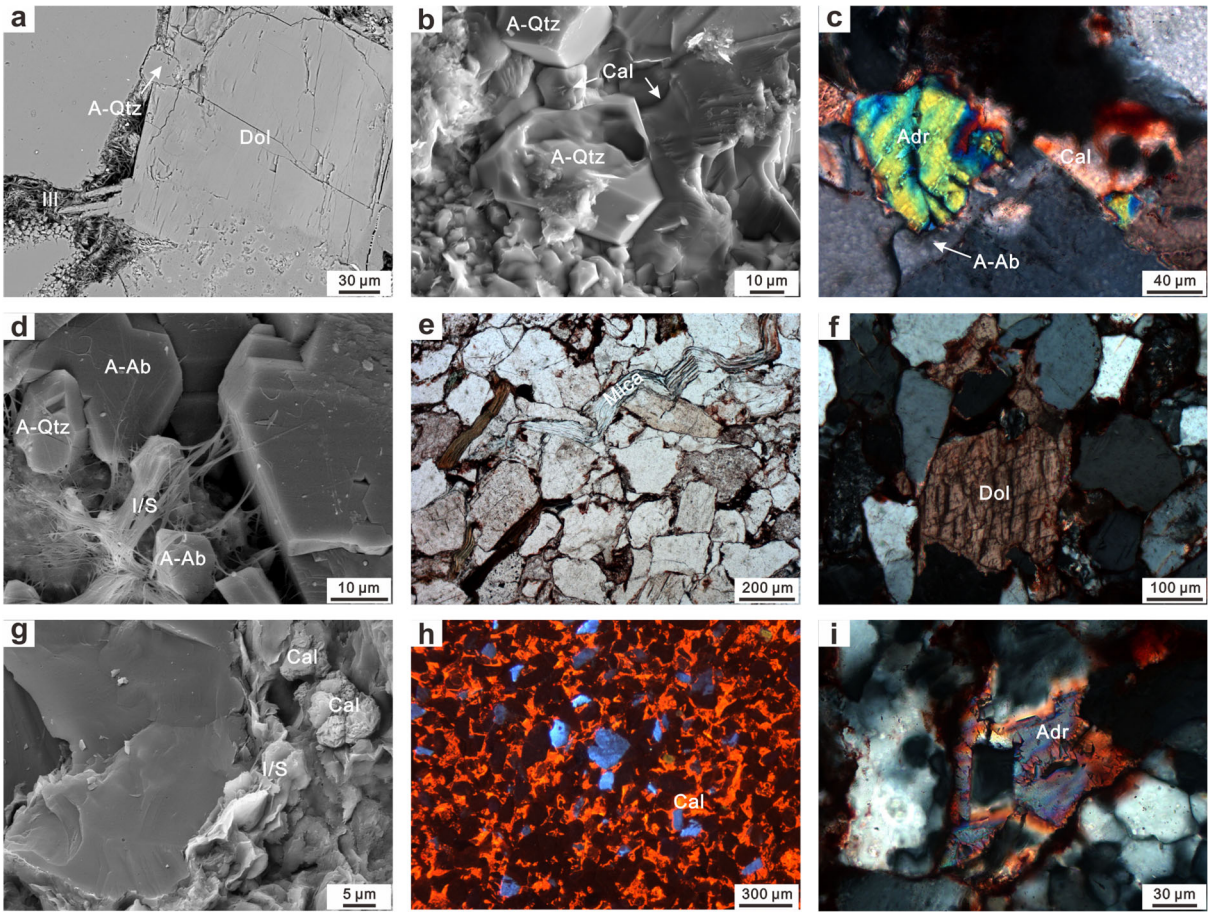


Figure 7. Diagenesis of different petrofacies: (**a**) dolomite postdates authigenic quartz and predates the precipitation of illite, petrofacies A, KS209, 6700.85 m, backscattered electron (BSE); (**b**) authigenic quartz fills pores and coexists with mixed-layer illite/smectite, predating the precipitation of calcite, petrofacies A, KS6, 5630.5 m, scanning electron microscopy (SEM); (**c**) pores filled with anhydrite, dolomite, and authigenic feldspar, where authigenic feldspar precipitated prior to anhydrite, petrofacies A, KS8, 6730 m, cross-polarized light (XPL); (**d**) authigenic feldspar, quartz, and mixed-layer illite/smectite precipitated in pores, petrofacies A, KS206, 6709.12 m, SEM; (**e**) mica deformed by compactional bending, petrofacies B, KS904, 7741 m, plane-polarized light (PPL); (**f**) trace carbonate minerals (dolomite) precipitated in pores, petrofacies B, KS904, 7732 m, XPL; (**g**) mixed-layer illite/smectite in pores, petrofacies B, KS501, 6364.22 m, SEM; (**h**) poikilotopic calcite cementation, petrofacies C, KS501, 6367.96 m, cathodoluminescence (CL); (**i**) minor anhydrite precipitation, petrofacies C, KS904, 7729.5 m, XPL. A-Qtz: authigenic quartz; Dol: dolomite; Cal: calcite; Adr: anhydrite; A-Ab: authigenic albite; I/S: mixed-layer illite/smectite.

In petrofacies C, the pores are extensively filled with carbonate minerals (Figure 7h). Petrographic features, such as poikilotopic cementation of calcite or dolomite, suggest the formation of carbonate minerals during early diagenesis. Although the presence of carbonate minerals enhances resistance to compaction during burial, pore space is already consumed by cementation. Like petrofacies B, late-stage fluid activity is weak, preventing large-scale dissolution and resulting in almost no effective porosity. Authigenic minerals are limited to calcite or dolomite, with only trace amounts of anhydrite sporadically replacing carbonate minerals or detrital grains.

4.2.4. Porosity and Permeability of Effective Reservoir Rocks and Tight Petrofacies

The porosity and permeability of different petrofacies are shown in Figure 8, which indicates that the ultra-deep tight sandstone reservoirs in the Keshen gas field are characterized by ultralow porosity and ultralow permeability. Although the sandstones are generally tight, relatively porous sandstones are still present within the reservoir. The porosity and permeability test results indicate that petrofacies A has relatively better petrophysical properties compared with petrofacies B and C. In the Cretaceous Bashijiqike Formation reservoirs, the porosities of petrofacies A range from 4% to 13.7%, with an average porosity of 7.3%, whereas its permeabilities vary between 0.01×10^{-3} μm^2 and 1.13×10^{-3} μm^2, averaging 0.15×10^{-3} μm^2 (Figure 8). In contrast, petrofacies B and petrofacies C present relatively poor petrophysical characteristics. Petrofacies B has porosities ranging from 1.6% to 5.2%, and the average porosity is 3.5%. The permeabilities of petrofacies B range from 0.01×10^{-3} μm^2 to 0.28×10^{-3} μm^2, and the average permeability is 0.04×10^{-3} μm^2 (Figure 8). Petrofacies C has porosities between 1.29% and 4.54%, and the average porosity is 2.8%. The permeabilities of petrofacies C range from 0.007×10^{-3} μm^2 to 0.13×10^{-3} μm^2, and the average permeability is 0.04×10^{-3} μm^2 (Figure 8).

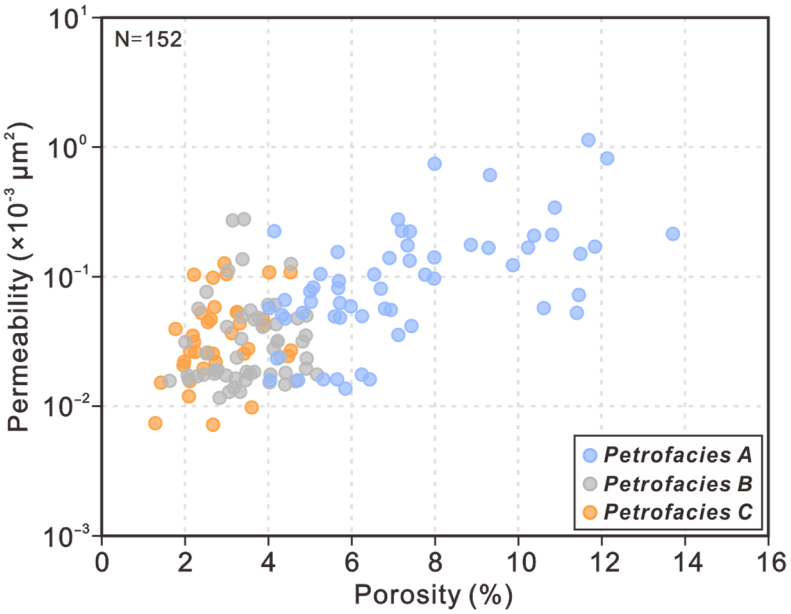


Figure 8. Petrophysical properties of the effective reservoir rock and tight petrofacies in the K_1bs ultra-deep tight sandstone reservoirs.

Based on the analysis of porosity and permeability across the three petrofacies, ductile grain-poor sandstone (petrofacies A) displays an average porosity approximately 5% higher than that of ductile grain-rich sandstone (petrofacies B) and carbonate–tightly cemented sandstone (petrofacies C), along with an average permeability that is one order of magnitude greater than that of the other two petrofacies. These results clearly demonstrate that, compared with the other two petrophysical facies, ductile grain-poor sandstone has significantly superior petrophysical properties. Consequently, ductile grain-poor sandstone is classified as an effective reservoir rock within ultra-deep tight sandstone reservoirs. In contrast, ductile grain-rich sandstone and carbonate–tightly cemented sandstone, which exhibit extremely poor petrophysical characteristics, are categorized as tight, non-reservoir petrofacies in ultra-deep tight sandstone reservoirs.

4.3. Effective Reservoir Rock Prediction Using Well Logging and Factor Analysis

4.3.1. Well Log Responses of Different Petrofacies

The values of the logging response corresponding to different petrofacies within the cored intervals were extracted according to the depth correction of well logs, standardization of well log data, and matching of core depths. Optimal well logs sensitive to various petrofacies types were selected via generating log crossplots and geostatistical analysis. Considering the differences in petrological composition, petrophysical properties, and diagenesis among different petrofacies, five conventional well logs were carefully chosen for identifying sandstone petrofacies in the ultra-deep tight sandstone reservoirs of the Keshen gas field. These five conventional logging curves are the gamma ray log (GR), which reflects the clay content; the acoustic log (AC), which indicates the rock porosity, degree of compaction, and fluid characteristics; the bulk density log (DEN); the neutron porosity log (CNL); and the resistivity log (RD).

Core observations and thin-section identification data were used to calibrate the logging responses of samples with confirmed petrofacies types. Crossplots of logging responses for different petrofacies were generated by extracting corresponding log values, as illustrated in Figure 9. Importantly, the vertical resolution of the well logs is 0.125 m. The logging responses of different petrofacies are shown in Table 4. Petrofacies A has low GR values ranging from 41.5 API to 66.6 API, with an average of 52.5 API, which is attributed to its low content of argillaceous lithic fragments, clay matrix, and authigenic clay minerals. Due to weak mechanical compaction, favorable porosity, and low bulk density, petrofacies A has moderate-to-high DT values between 54.0 μs/ft and 64.9 μs/ft (average of 58.8 μs/ft), moderate-to-low DEN values ranging from 2.48 g/cm^3 to 2.63 g/cm^3 (average of 2.55 g/cm^3), low RD values between 15.3 Ω·m and 53.5 Ω·m (average of 33.5 Ω·m), and low CNL values ranging from 0.9% to 6.7% (average of 3.4%). In contrast, petrofacies B has moderate-to-high GR values, moderate-to-high CNL values, moderate-to-low DT values, high DEN values, and low RD values. Petrofacies C is characterized by moderate GR values, moderate CNL values, extremely low DT values, high DEN values, and variable RD values, as shown in Figure 9.

Table 4. Logging responses of different lithofacies of effective reservoir rocks and tight petrofacies.

Logging Responses	Petrofacies A (Effective Reservoir Rocks)		Petrofacies B (Tight Petrofacies)		Petrofacies C (Tight Petrofacies)	
	Range	Average	Range	Average	Range	Average
GR (API)	41.5–66.6	52.5	63.3–101.6	79.1	50.4–78.9	64.4
AC (μs/ft)	54.0–64.9	58.8	55.1–62.6	58.1	53.2–59.8	55.9
DEN (g/cm^3)	2.48–2.63	2.55	2.57–2.66	2.61	2.59–2.70	2.63
RD (Ω·m)	15.3–53.5	33.5	10.3–40.5	27.0	12.7–61.2	30.1
CN (%)	0.9–6.7	3.4	2.3–7.8	5.1	2.2–7.3	4.2

Although crossplot analysis of log data reveals distinguishable differences in logging response characteristics among the three petrofacies, partial overlaps in log data between different petrofacies prevent the precise differentiation of their logging signatures. For example, petrofacies B and petrofacies C exhibit nearly identical density log ranges. These overlaps indicate that relying exclusively on log crossplots is insufficient to effectively distinguish the logging responses of the three petrofacies.

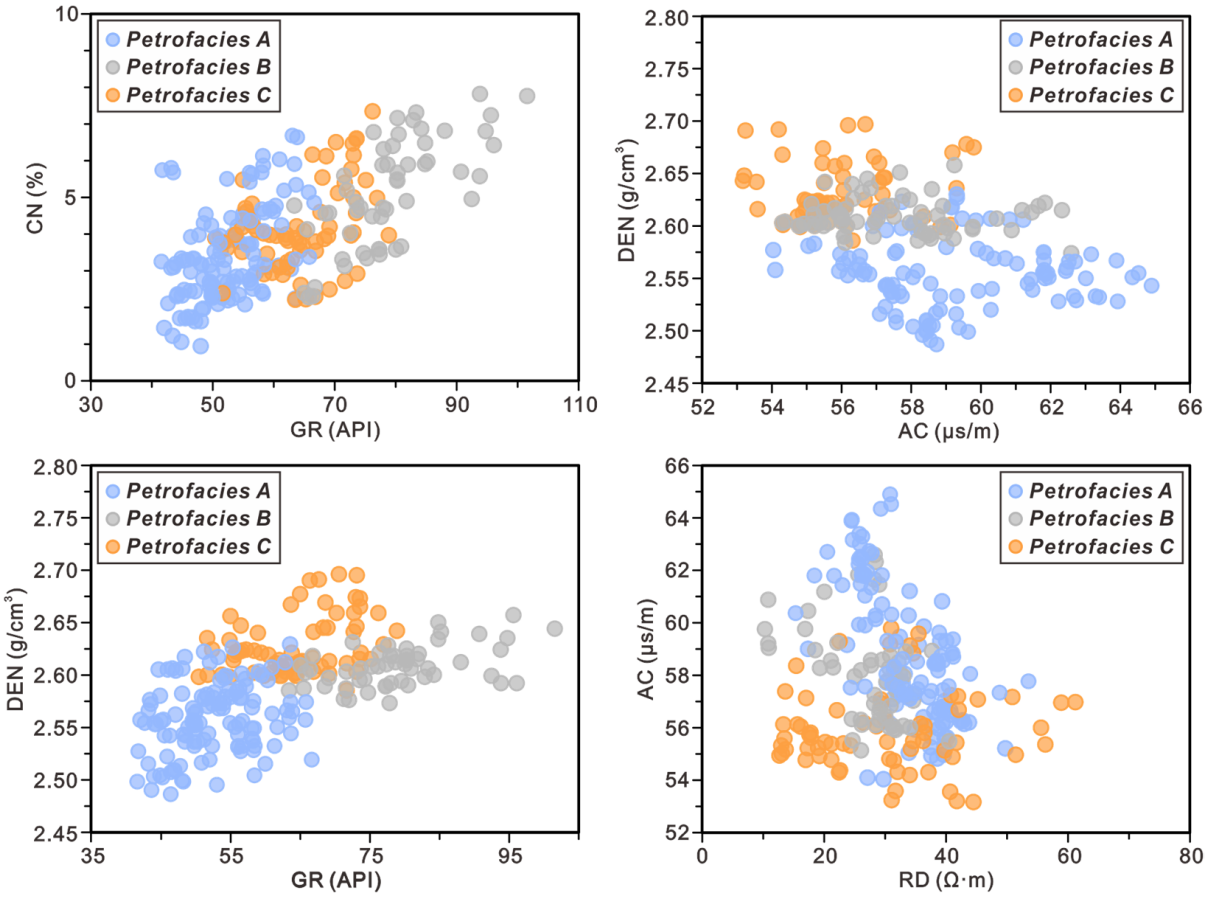


Figure 9. Intersection of well logs of different petrofacies in the K_1bs ultra-deep tight sandstone reservoirs.

4.3.2. Factor Analysis of the Well Log Responses of Different Petrofacies

Principal component analysis yielded two factors, F1 and F2, with values of 2.126 and 1.479, respectively, collectively accounting for 87.672% of the cumulative variance. The coefficients corresponding to each parameter within the factors, representing eigenvectors, were derived by dividing the explanatory power of each factor over the original variables by the square root of its respective eigenvalue. These eigenvectors were then multiplied by the standardized data matrix, and by incorporating the mathematical relationships between the standardized and raw data, the expressions for the two factors were formulated as follows:

$$F1 = 0.610 \times ZGR + 0.542 \times ZCN - 0.060 \times ZDT + 0.499 \times ZDEN - 0.288 \times ZLnRD \quad (1)$$

$$F2 = -0.093 \times ZGR + 0.335 \times ZCN + 0.733 \times ZDT - 0.405 \times ZDEN - 0.421 \times ZLnRD \quad (2)$$

where ZGR represents the normalized gamma ray (API), ZCN denotes the normalized compensated neutron porosity (%), ZAC corresponds to the normalized acoustic velocity (μs/ft), ZDEN signifies the normalized bulk density (g/cm^3), and ZLnRD indicates the normalized logarithm of resistivity (Ω·m).

Eigenvalues for distinct petrofacies were computed using these aforementioned formulas. For ductile grain-poor sandstone, the F1 values range from −2.64 to 0.76, with a mean of −1.13, whereas the F2 values range from −2.04 to 3.14, with a mean of 0.35. The ductile grain-rich sandstones present F1 values between −0.24 and 3.99 (mean of 1.59) and F2 values between −1.13 and 2.17 (mean of 0.23). The carbonate-tightly cemented sandstone samples present F1 values ranging from −0.63 to 2.75 (mean of 0.80) and F2 values ranging from −2.47 to 0.68 (mean of −0.84). A crossplot analysis of principal factors

F1 and F2 (Figure 10) demonstrated effective petrofacies differentiation through factor analysis, with distinct eigenvalue distributions observed across petrofacies. Validation using cored wells containing abundant samples with confirmed petrofacies classifications reveals an agreement rate of 85.3% between the predictions generated by the model and manual interpretations for ductile grain-poor sandstone, ductile grain-rich sandstone, and carbonate–tightly cemented sandstone.

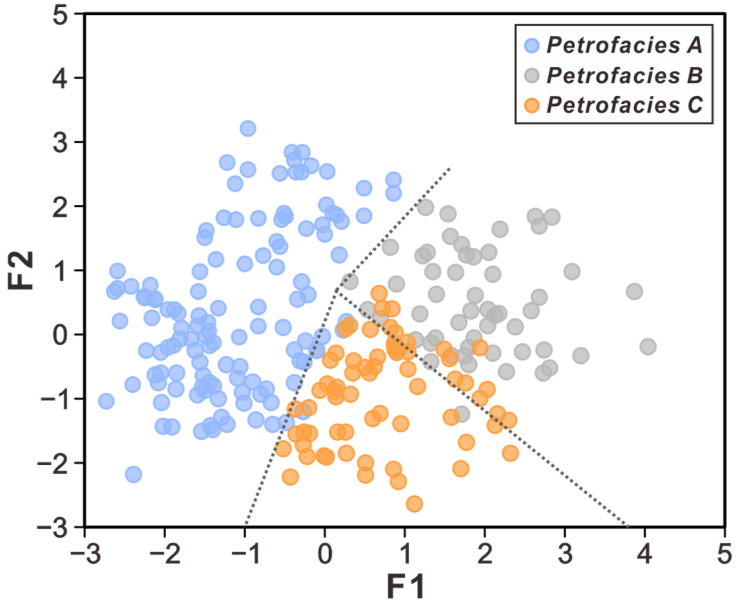


Figure 10. Diagram showing the intersection of two factors influencing the well log parameters of the effective reservoir rock and tight petrofacies in the K_1bs ultra-deep tight sandstone reservoirs.

4.3.3. Prediction of Effective Reservoir Rocks in Wells

The predictive model was implemented to forecast the spatial distribution of effective reservoir rocks and tight petrofacies within the ultra-deep tight sandstone reservoirs of the Cretaceous Bashijiqike Formation in wells in the Keshen gas field, and it is presented in Figure 11. The predictive results from the wells reveal an interbedded distribution of three petrofacies within the reservoirs. Ductile grain-poor sandstone, which serves as a potential effective reservoir unit, is interbedded with tight petrofacies, including ductile grain-rich sandstone and carbonate–tightly cemented sandstone. This lithological architecture results in limited connectivity of effective reservoir bodies within ultra-deep tight sandstone reservoirs.

The ultra-deep tight sandstone reservoirs exhibit heterogeneity at different scales. Sand bodies are stratigraphically segregated by argillaceous intervals, forming a primary framework of lithological heterogeneity between sandstone and mudstone. Furthermore, intrasand body structural heterogeneity is characterized by the juxtaposition of ductile grain-poor sandstone with relatively favorable petrophysical properties and adjacent tight petrofacies, such as ductile grain-rich sandstone and carbonate–tightly cemented sandstone.

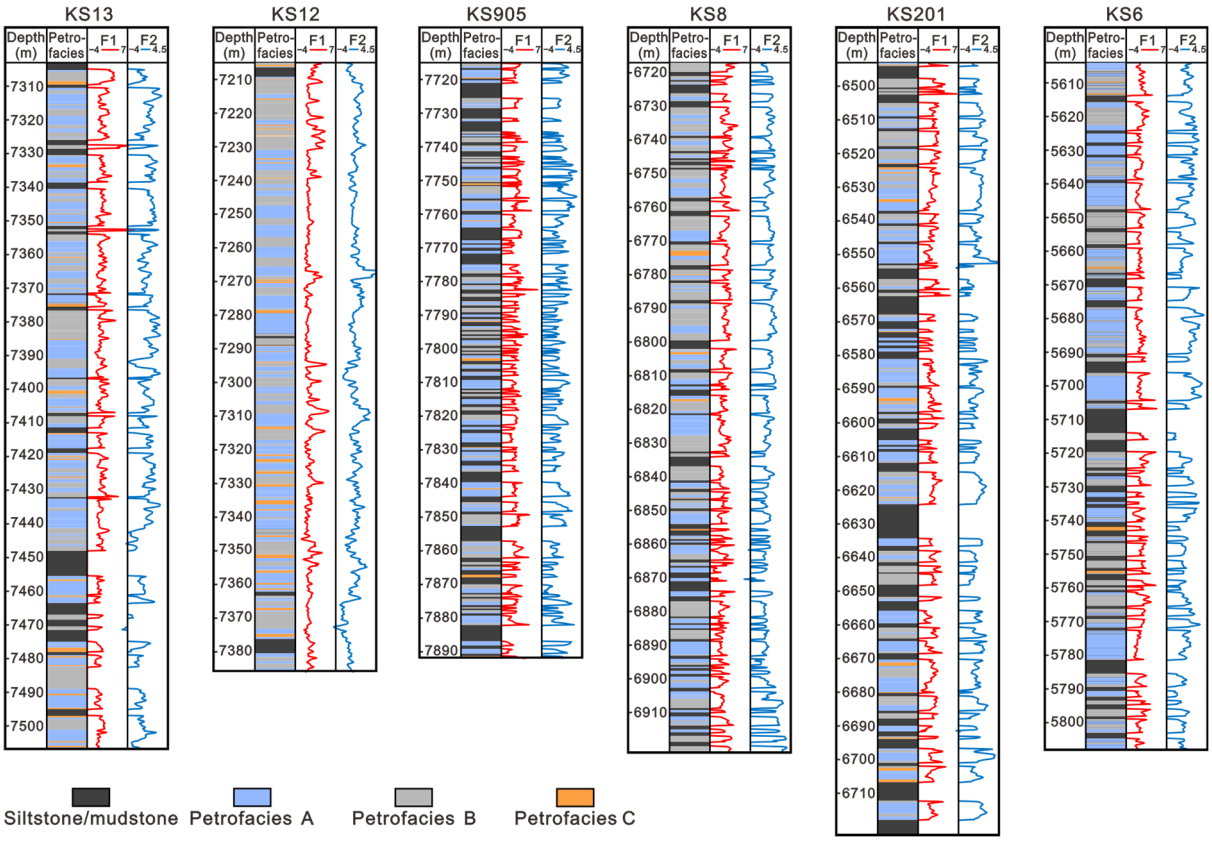


Figure 11. Effective reservoir rock and tight petrofacies well log prediction of the K_1bs ultra-deep tight sandstone reservoirs.

5. Discussion

Previous studies have recognized that heterogeneity, as a fundamental attribute of clastic rock formations, is universally present across different scales [7,31,34]. Ultra-deep sandstone reservoirs have undergone intense mechanical compaction and multiple stages of cementation and dissolution during burial processes, resulting in more pronounced pore-scale heterogeneity [35,36]. The differential petrophysical properties exhibited by various sandstones during deep burial processes are attributed to the combined controlling effects of the sediment source, sedimentation, tectonic movements, and diagenesis [37].

For one reservoir unit, different positions within a sand body may experience completely distinct diagenetic evolutionary pathways, leading to significant variations in pore systems and petrophysical properties within sandstones [38]. Previous studies have suggested that the enhanced petrophysical properties in tight sandstone reservoirs are related to the development of primary pores, secondary pores, and natural fractures [39]. During the shallow burial stages of ultra-deep tight sandstone reservoirs, sandstones undergo early diagenesis. Ductile grain-rich sandstones lose pore space under intense mechanical compaction and their permeability gradually becomes low. This results in a weak interaction between fluid and rock in these sandstones, leading to a low content of cementation. Carbonate-cemented tight sandstones often develop at the fluid active configuration interfaces between sand bodies and tend to cause extensive precipitation of carbonate minerals during the early diagenetic stage [33]. Locally developed carbonate-cemented tight sandstones in the reservoir nearly exhaust their primary porosity at this stage, with the rock becoming extremely tight. These early-stage tight rocks rarely undergo further diagenetic alterations during deep burial, rarely exhibit secondary dissolution pores, and demonstrate weak fluid—rock interactions in deep burial stages.

In contrast, ductile grain-poor sandstones exhibit relatively weak mechanical compaction, weak cementation, and strong dissolution characteristics. During burial processes, these sandstones maintain relatively active fluid flow, where unstable components such as feldspar and lithic fragments undergo dissolution, whereas authigenic quartz, feldspar, and clay minerals precipitate in pores with low total cement contents. Although ultra-deep reservoirs generally tend toward tight sandstone, effective reservoir rocks with relatively good porosity and permeability still exist, providing space for hydrocarbon accumulation and migration. The heterogeneous distribution of effective reservoirs and non-productive sandstones in tight sandstone reservoirs is common [40]. The degree of development and spatial distribution of these effective reservoir rocks constitute the critical foundation for hydrocarbon enrichment in ultra-deep reservoir [41]. However, the development of effective reservoir rocks does not guarantee geological fluid migration in ultra-deep tight sandstones. The presence of argillaceous rocks and tight petrofacies in ultra-deep reservoirs may act as barriers, hindering the hydrocarbon migration. This dual-scale heterogeneity—interbedded sand—mud sequences and intrasand petrofacies variations—collectively governs the complex fluid flow behavior and reservoir quality distribution within the ultra-deep tight sandstone system.

6. Conclusions

In this study, three sandstone petrofacies within ultra-deep tight gas reservoirs were classified. Based on comparative analysis of the detrital texture and mineralogy, interstitial material, diagenesis, and petrophysical properties (porosity and permeability) across distinct petrofacies, the differences between three petrofacies were analyzed. The results of this research clarified the types of effective reservoir rocks and tight petrofacies within ultra-deep tight sandstone reservoirs. An integrated methodology incorporating core analysis, microscopic observations, well logging, and factor analysis enabled the establishment of predictive models for the identification of effective reservoir rocks and tight petrofacies in ultra-deep tight sandstone reservoirs. The main research findings are summarized as follows:

1. The classification of sandstone types within the ultra-deep reservoirs of the Keshen gas field, which was performed based on detrital grain texture and mineralogy, interstitial material, diagenesis, and pore characteristics, resulted in the division of three distinct petrofacies. Petrofacies A corresponds to ductile grain-poor sandstone, petrofacies B corresponds to ductile grain-rich sandstone, and petrofacies C corresponds to carbonate–tightly cemented sandstone. Among these sandstones, petrofacies A represents the effective reservoir rock type, whereas petrofacies B and petrofacies C constitute the tight petrofacies.
2. Petrofacies A features relatively coarse grain sizes, moderate mechanical compaction, diverse but low-abundance authigenic minerals, and well-developed primary and secondary pores, with porosities ranging from 4% to 13.7% and permeabilities ranging from 0.01×10^{-3} μm^2 to 1.13×10^{-3} μm^2. Petrofacies B features abundant compaction-susceptible ductile grains, intense mechanical compaction, underdeveloped authigenic minerals and pores, minimal dissolution evidence, porosities of 1.6–5.2%, and permeabilities between 0.01×10^{-3} μm^2 and 0.28×10^{-3} μm^2. Petrofacies C features pervasive carbonate cementation, a poikilotopic texture, negligible authigenic mineral content, no dissolution, poorly developed pore systems with porosities ranging from 1.29% to 4.54%, and permeabilities ranging from 0.007×10^{-3} μm^2 to 0.13×10^{-3} μm^2.
3. Sandstone petrofacies identified through core analysis and microscopic testing were integrated with well log and factor analyses. Through the evaluation of well log signa-

tures across the petrofacies types, five sensitive logging parameters were optimized: gamma ray (GR), acoustic (AC), bulk density (DEN), neutron porosity (CNL), and resistivity (RD). Factor analysis facilitated the development of petrofacies prediction models, enabling the spatial mapping of effective reservoir rocks and tight lithofacies distributions. The models reveal an interbedded architecture in which ductile grain-poor sandstone (effective reservoirs) is interbedded with ductile grain-rich sandstone and carbonate-tightly cemented sandstone (tight petrofacies), resulting in the restricted connectivity of reservoir units and pronounced reservoir heterogeneity.

Author Contributions: Conceptualization, Z.L. and X.F.; methodology, Z.L. and X.L.; validation, X.S.; formal analysis, Z.L. and X.S.; investigation, Z.L.; resources, X.L.; data curation, H.W.; writing—original draft preparation, Z.L.; writing—review and editing, X.S.; visualization, X.S.; supervision, X.L. and X.F.; funding acquisition, Z.L. and X.S. All authors have read and agreed to the published version of the manuscript.

Funding: This research was funded by the Natural Science Foundation of Heilongjiang Province (Grant No. LH2022D009), the National Natural Science Foundation of China (Grant No. 42202156), the China Postdoctoral Science Foundation (Grant No. 2024M750397), and the Heilongjiang Postdoctoral Fund (Grant No. LBH-Z24102).

Data Availability Statement: The original contributions presented in the study are included in the article, further inquiries can be directed to the corresponding author.

Acknowledgments: The authors are particularly grateful to PetroChina Tarim Oil Field Company, PetroChina, for providing the primary geological data.

Conflicts of Interest: The authors declare no conflicts of interest.

References

1. Li, Q.C.; Li, Q.; Wu, J.J.; Li, X.Z.; Li, H.B.; Cheng, Y.F. Wellhead stability during development process of hydrate reservoir in the Northern South China Sea: Evolution and mechanism. *Processes* **2024**, *13*, 40. [CrossRef]
2. Li, Q.; Li, Q.C.; Cao, H.Q.; Wu, J.J.; Wang, F.L.; Wang, Y.L. The crack propagation behaviour of CO_2 fracturing fluid in unconventional low permeability reservoirs: Factor analysis and mechanism revelation. *Processes* **2025**, *13*, 159. [CrossRef]
3. Ehrenberg, S.N.; Nadeau, P.H. Sandstone vs. carbonate petroleum reservoirs: A global perspective on porosity—depth and porosity-permeability relationships. *AAPG Bull.* **2005**, *89*, 435–445. [CrossRef]
4. Morad, S.; Ketzer, J.M.; De Ros, L.F. Spatial and temporal distribution of diagenetic alterations in siliciclastic rocks: Implications for mass transfer in sedimentary basins. *Sedimentology* **2000**, *47*, 95–120. [CrossRef]
5. Morad, S.; Al-Ramadan, K.; Ketzer, J.M.; De Ros, L.F. The impact of diagenesis on the heterogenity of sandstone reservoirs: A review of the role of depositional facies and sequence stratigraphy. *AAPG Bull.* **2010**, *94*, 1267–1309. [CrossRef]
6. Worden, R.H.; Morad, S. Clay minerals in sandstones: Controls on formation, distribution and evolution. In *Clay Mineral Cement in Sandstones*; Worden, R.H., Morad, S., Eds.; Special Publication 34; International Association of Sedimentologists: Oxford, UK; Wiley Blackwell Publishing: Hoboken, NJ, USA, 2003; pp. 3–41.
7. Taylor, T.R.; Giles, M.R.; Hathon, L.A.; Diggs, T.N.; Braunsdorf, N.R.; Birbiglia, G.V.; Kittridge, M.G.; Macaulay, C.I.; Espejo, I.S. Sandstone diagenesis and reservoir quality prediction: Models, myths, and reality. *AAPG Bull.* **2010**, *94*, 1093–1132. [CrossRef]
8. Pittman, E.D.; Larese, R.E. Compaction of lithic sands: Experimental results and applications. *AAPG Bull.* **1991**, *75*, 1279–1299.
9. Bloch, S.; Lander, R.H.; Bonnell, L. Anomalously high porosity and permeability in deeply buried sandstone reservoirs: Origin and predictability. *AAPG Bull.* **2002**, *86*, 301–328.
10. Mousavi, M.A.; Bryant, S.L. Geometric models of porosity reduction by ductile grain compaction and cementation. *AAPG Bull.* **2013**, *97*, 2129–2148. [CrossRef]
11. Lander, R.H.; Walderhaug, O. Predicting porosity through simulating sandstone compaction and quartz cementation. *AAPG Bull.* **1999**, *83*, 433–449.
12. Walderhaug, O.; Bjørkum, P.A.; Aase, N.E. Kaolin-coating of stylolites, effect on quartz cementation and general implications for dissolution at mineral interfaces. *J. Sediment. Petrol.* **2006**, *76*, 234–243. [CrossRef]
13. Lander, R.H.; Larese, R.E.; Bonnell, L.M. Toward more accurate quartz cement models: The importance of euhedral versus noneuhedral growth rates. *AAPG Bull.* **2008**, *92*, 1537–1563. [CrossRef]

14. Worden, R.H.; Oxtoby, N.H.; Smalley, P.C. Can oil emplacement prevent quartz cementation in sandstones? *Pet. Geosci.* **1998**, *4*, 129–137. [CrossRef]
15. Marchand, A.M.E.; Haszeldine, R.S.; Smalley, P.C.; Macaulay, C.I.; Fallick, A.E. Evidence for reduced quartz cementation rates in oil-filled sandstones. *Geology* **2001**, *29*, 915–918. [CrossRef]
16. Bjørlykke, K.; Jahren, J. Open or closed geochemical system during diagenesis insedimentary basin: Constraints on mass transfer during diagenesis and the prediction of porosity in sandstone and carbonate reservoirs. *AAPG Bull.* **2012**, *96*, 2193–2214. [CrossRef]
17. Cumella, S.P.; Scheevel, J.; Camp, W.K. The influence of stratigraphy and rock mechanics on Mesaverde gas distribution, Piceance Basin, Colorado. In *Understanding, Exploring, and Developing Tight-Gas Sands—2005 Vail Hedberg Conference: AAPG Hedberg Series*; American Association of Petroleum Geologists: Tulsa, OK, USA, 2008; Volume 9, pp. 137–155.
18. Zeng, L.B.; Li, X.Y. Fractures in sandstone reservoirs with ultra-low permeability: A case study of the Upper Triassic Yanchang Formation in the Ordos Basin, China. *AAPG Bull.* **2009**, *93*, 461–477.
19. Ameen, M.S.; MacPherson, K.; Al-Marhoon, M.I.; Rahim, Z. Diverse fracture properties and their impact on performance in conventional and tight-gas reservoirs, Saudi Arabia: The Unayzah, South Haradh case study. *AAPG Bull.* **2012**, *96*, 459–492. [CrossRef]
20. Grigsby, J.D.; Langford, R.P. Effects of diagenesis on enhanced-resolution bulk density logs in Tertiary Gulf Coast sandstones: An example from the lower Vicksburg Formation, McAllen Ranch field, south Texas. *AAPG Bull.* **1996**, *80*, 1801–1819.
21. Ozkan, A.; Cumella, S.P.; Milliken, K.L.; Laubach, S.E. Prediction of lithofacies and reservoir quality using well logs, late cretaceous williams fork formation, Mamm creek field, Piceance Basin, Colorado. *AAPG Bull.* **2011**, *95*, 1699–1723. [CrossRef]
22. Lai, J.; Wang, G.W.; Wang, S.; Cao, J.T.; Li, M.; Pang, X.J.; Zhou, Z.L.; Fan, X.Q.; Dai, Q.Q.; Yang, L.; et al. Review of diagenetic facies in tight sandstones: Diagenesis, diagenetic minerals, and prediction via well logs. *Earth-Sci. Rev.* **2018**, *185*, 234–258. [CrossRef]
23. Qiu, N.S.; Chang, J.; Zuo, Y.H.; Wang, J.Y.; Li, H. Thermal evolution and maturation of lower Paleozoic source rocks in the Tarim Basin, northwest China. *AAPG Bull.* **2012**, *96*, 789–821. [CrossRef]
24. Jia, C.Z.; Gu, J.Y.; Zhang, G.Y. Geological constraints of giant and medium-sized gas fields in Kuqa Depression. *Chin. Sci. Bulletin.* **2002**, *47*, 47–54, (In Chinese with English abstract). [CrossRef]
25. Song, Y.; Zhao, M.J.; Liu, S.B.; Qin, S.F.; Hong, F. Features of hydrocarbon accumulation in three types of foreland basins in China. *Petrol. Explor. Dev.* **2005**, *32*, 1–6.
26. Wang, Z.M. Formation mechanism and enrichment regularities of Kelasu subsalt deep large gas field in Kuqa Depression, Tarim Basin. *Nat. Gas Geosci.* **2014**, *25*, 153–166, (In Chinese with English abstract).
27. Lai, J.; Wang, G.W.; Yu, C.; Wu, Q.K.; Zhang, X.T.; Sun, Y.H. Deep burial diagenesis and reservoir quality evolution of high-temperature, high-pressure sandstones: Examples from lower Cretaceous Bashijiqike formation in Keshen area, Kuqa depression, Tarim basin of China. *AAPG Bull.* **2017**, *101*, 829–862. [CrossRef]
28. Zhang, S.C.; Zhang, B.; Zhu, G.Y.; Li, Z.X. Geochemical evidence for coal-derived hydrocarbons and their charge history in the Dabei Gas Field, Kuqa Thrust Belt, Tarim Basin, NW China. *Mar. Pet. Geol.* **2011**, *28*, 1364–1375. [CrossRef]
29. Guan, S.W.; Chen, Z.X.; Li, B.L. Discussions on the character and interpretation model of Kelasu deep structures in the Kuqa area. *Petrol. Explor. Dev.* **2010**, *37*, 531–536.
30. Li, Y.; Guo, S.; Wang, X.; Hou, Y.F.; Neng, Y.; Wang, Z.X.; Zhou, L.; Yang, W.J.; Tan, C. Stratification model of an ultradeep tight sandstone fracture reservoir under tectonic stress: A case study of a Cretaceous reservoir in the Kuqa foreland thrust belt of the Tarim Basin. *J. Nat. Gas. Sci. Eng.* **2017**, *45*, 53–64. [CrossRef]
31. Zhang, H.L.; Zhang, R.H.; Yang, H.J.; Shou, J.F.; Wang, J.P.; Liu, C.; Chen, G. Characterization and evaluation of ultra-deep fracture-pore tight sandstone reservoirs: A case study of Cretaceous Bashijiqike Formation in Kelasu tectonic zone in Kuqa foreland basin, Tarim, NW China. *Petrol. Explor. Dev.* **2014**, *41*, 158–167. [CrossRef]
32. Shi, H.; Luo, X.R.; Yang, H.J.; Lei, G.L.; Tang, Y.G.; Zhang, L.K.; Lei, Y.H. Sources of quartz grains influencing quartz cementation and reservoir quality in ultra-deeply buried sandstones in Keshen-2 gas field, north-west China. *Mar. Pet. Geol.* **2018**, *98*, 185–198. [CrossRef]
33. Cao, B.F.; Sun, W.; Li, J. Reservoir petrofacies-a tool for characterization of reservoir quality and pore structures in a tight sandstone reservoir: A study from the sixth member of upper triassic yanchang formation, Ordos Basin, China. *J. Pet. Sci. Eng.* **2021**, *199*, 108294. [CrossRef]
34. Scorgie, J.C.; Worden, R.H.; Utley, J.E.P.; Roche, I.P. Reservoir quality and diagenesis of Triassic sandstones and siltstones from arid fluvial and playa margin environments: A study of one of the UK's earliest producing oilfields. *Mar. Petrol. Geol.* **2021**, *131*, 105154. [CrossRef]
35. Pettijohn, F.J.; Potter, P.E.; Siever, R. *Sand and Sandstone*; Springer Science & Business Media: Berlin, Germany, 2012.
36. Fitch, P.J.R.; Lovell, M.A.; Davies, S.J.; Pritchard, T.; Harvey, P.K. An integrated and quantitative approach to petrophysical heterogeneity. *Mar. Pet. Geol.* **2015**, *63*, 82–96. [CrossRef]
37. Bjørlykke, K. Relationships between depositional environments, burial history and rock properties. Some principal aspects of diagenetic process in sedimentary basins. *Sediment. Geol.* **2014**, *301*, 1–14. [CrossRef]

38. Luo, X.R.; Zhang, L.Q.; Zhang, L.Q.; Lei, Y.H.; Cheng, M.; Shi, H.; Cao, B.F. Heterogeneity of clastic carrier bed and hydrocarbon migration and accumulation. *Acta Pet. Sin.* **2020**, *41*, 253–272, (In Chinese with English abstract).
39. Weisenberger, T.B.; Eichhubl, P.; Laubach, S.E.; Fall, A. Degradation of fracture porosity in sandstone by carbonate cement, Piceance Basin, Colorado USA. *Pet. Geosci.* **2019**, *25*, 354–370. [CrossRef]
40. Khan, M.A.; Khan, T.; Ali, A.; Bello, A.M.; Radwan, A.E. Role of depositional and diagenetic controls on reservoir quality of complex heterogenous tidal sandstone reservoirs: An example from the Lower Goru formation, Middle Indus Basin Southwest Pakistan. *Mar. Petrol. Geol.* **2023**, *154*, 106337. [CrossRef]
41. Schmoker, J.W. Resource-assessment perspectives for unconventional gas systems. *AAPG Bull.* **2002**, *86*, 1993–1999.

Disclaimer/Publisher's Note: The statements, opinions and data contained in all publications are solely those of the individual author(s) and contributor(s) and not of MDPI and/or the editor(s). MDPI and/or the editor(s) disclaim responsibility for any injury to people or property resulting from any ideas, methods, instructions or products referred to in the content.